JACS
JOURNAL OF THE AMERICAN CHEMICAL SOCIETY
Article
pubs.acs.org/JACS

Nanoscale-Phase-Separated Pd–Rh Boxes Synthesized via Metal Migration: An Archetype for Studying Lattice Strain and Composition Effects in Electrocatalysis

Brian T. Sneed,[†,‡] Casey N. Brodsky,[†,‡] Chun-Hong Kuo,[‡] Leo K. Lamontagne,[‡] Ying Jiang,[§] Yong Wang,[§] Franklin (Feng) Tao,[⊥] Weixin Huang,[⊥] and Chia-Kuang Tsung*[,‡]

[‡]Department of Chemistry, Merkert Chemistry Center, Boston College, 2609 Beacon Street, Chestnut Hill, Massachusetts 02467, United States

[§]Center of Electron Microscopy and State Key Laboratory of Silicon Materials, Department of Materials Science and Engineering, Zhejiang University, Hangzhou 310027, China

[⊥]Department of Chemistry and Biochemistry, University of Notre Dame, Notre Dame, Indiana 46556, United States

Supporting Information

ABSTRACT: Developing syntheses of more sophisticated nanostructures comprising late transition metals broadens the tools to rationally design suitable heterogeneous catalysts for chemical transformations. Herein, we report a synthesis of Pd–Rh nanoboxes by controlling the migration of metals in a core–shell nanoparticle. The Pd–Rh nanobox structure is a grid-like arrangement of two distinct metal phases, and the surfaces of these boxes are {100} dominant Pd and Rh. The catalytic behaviors of the particles were examined in electrochemistry to investigate strain effects arising from this structure. It was found that the trends in activity of model fuel cell reactions cannot be explained solely by the surface composition. The lattice strain emerging from the nanoscale separation of metal phases at the surface also plays an important role.

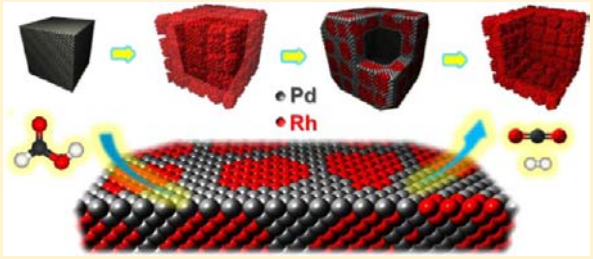

INTRODUCTION

The ability to control the electronic surface structure of metal nanoparticles affords us access to materials that can be examined for fundamental understanding of heterogeneous catalysis.[1] It has been demonstrated that modification of the electronic surface structure of metal nanoparticle catalysts can be accomplished by establishing atomic-level control over crystal facets,[2] composition,[3] and lattice strain.[4] The lattice strain effect on catalysis has attracted great attention recently. Lattice strain in a nanoparticle can be generated by the lattice mismatch in a core–shell nanostructure or twinned structures.[4,5] The use of bimetallic core–shell nanoparticles in electrochemical catalysis is advantageous due to the variety of structures and compositions that can be accessed.[6−8] There are now synthetic routes to hollow,[9−12] core–shell,[13,14] alloy,[15] yolk–shell,[16,17] and multishelled[6] type nanostructures with multiple components. The possibility of creating additional surface area through the introduction of pores and cavities in porous or hollow nanostructures is also attractive for catalytic applications. Many have aimed at producing bimetallic hollow nanostructures comprising platinum group metals because of their high activity and stability as electrocatalysts.[18−21] Control of Pt–Pd bimetallic nanostructures has been heavily pursued because of enhanced activity as the catalytic material for electrooxidations and reductions in fuel-cell research.[3,9,22,23]

Rhodium is another platinum group metal that has been investigated as an electrocatalytic material.[21,24−34] The chemical stability of rhodium films is greatly increased compared with other platinum group metals (PGM) and has been utilized in microelectronics.[35,36] The synthesis of nanoparticles with control of the Rh surface, however, remains challenging because of its propensity toward forming disordered nanostructures.[37] Many works have exhibited dendritic,[38] horned,[25] aggregated,[39] or networked[25,29] nanostructures of Rh that are either polycrystalline, exposing random crystal facets, or are otherwise without much long-range order. Pioneering examples demonstrate the synthesis of Rh cubic and octahedral structures,[40−43] but these examples show that there is still ample room for improvement of nanoscale control of particles comprising Rh.

Herein, we report a synthesis of shape-controlled Pd–Rh nanoboxes and Rh nanoframeworks by controlling metal migration at the atomic level, and we describe in detail their characterization, mechanisms for formation, and catalytic behaviors. Utilizing metal migration in a nanoparticle has been demonstrated as a way to achieve atomic level structural control.[44−46] In recent years, this concept has been used to control Rh structures. Zhang et al. demonstrated the sacrificial

Received: May 29, 2013
Published: August 26, 2013

dx.doi.org/10.1021/ja405387q | J. Am. Chem. Soc. 2013, 135, 14691−14700

replacement of Rh by Pd to generate hollow Pd cubes with Rh cubes in the interior.[47] Xie et al. have shown that removal of cubic Pd cores from Pd−Rh core−nanoframes can produce pure Rh nanoframes with high surface area and a degree of facet control.[38,48] This is achieved by oxidative etching with the addition of $HCl/FeCl_3$ and accelerated by the formation of halide complexes. Relatedly, a surface detachment−readhesion mechanism promoted by metal−halide complexes has also been proposed and studied in the synthesis of monometallic Rh nanocubes.[49]

Our group has previously contributed an aqueous phase procedure for the synthesis of bimetallic Pd−Rh core−island-shell nanoparticles with control of Rh surface using shape-directing substrates and halide ions.[31] Using this information, we take advantage of the Pd−Rh heterostructures to create new structures in this work. Instead of directly influencing the Rh during nucleation and growth, we are able to control the migration of the Pd in bimetallic particles postsynthesis. The migration treatment of the core−shell nanoparticles at raised temperatures without the addition of an etchant or reducing agent generated hollow bimetallic Pd−Rh nanoboxes with smooth faceting, while the addition of an etchant generated hollow Rh nanostructures consisting of a fused-island framework. The Pd nanoparticles, Pd−Rh core−shell nanostructures, Pd−Rh nanoboxes, and Rh nanoframeworks were then examined and compared for activity in CO-stripping, formic acid oxidation (FOR), ethanol oxidation (EOR), and oxygen reduction (ORR) electrocatalysis. The activity for these model fuel cell reactions is then used to link the factors of lattice strain and composition in the nanostructures to their catalytic behaviors.

RESULTS AND DISCUSSION

The synthesis of Pd−Rh nanoboxes (NBs) and Rh nanoframeworks (NFWs) by manipulation of Pd migration in Pd−Rh core−island-shell nanocubes (NCs) is depicted in Scheme 1.

Scheme 1. Illustration of the Synthesis of Pd−Rh Nanoboxes and Rh Cubic Nanoframeworks from Core−Island-Shell NCs with Heating under Different Redox Environments

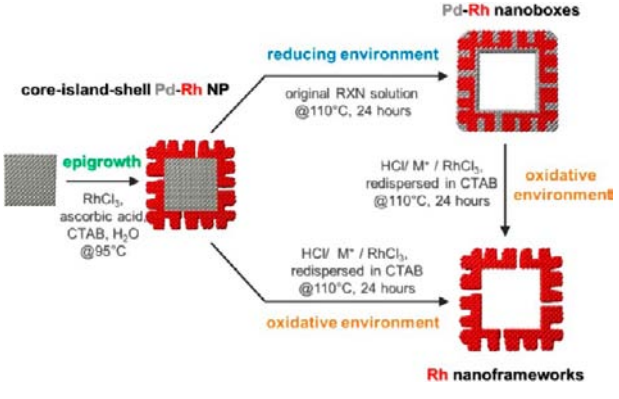

First, Pd−Rh core−island-shell nanocubes were synthesized as described by our previous work. Next, the core−island-shell nanocubes undergo transformation to either Pd−Rh NBs or Rh NFWs through alternate pathways involving migration and oxidative etching of the Pd cubic core. Under migration treatment by moving the original core−island-shell reaction solution to a pressure vessel at a raised temperature, Pd atoms relocated from the core to the gaps between surfaces of the Rh framework overgrowth. The process recapitulated a cubic outer surface and resulted in the Pd−Rh NBs. In the formation of Rh NFWs from core−shell NPs, the Pd can then be selectively removed from the NBs by addition of an etchant such as dilute hydrochloric acid or metal ions to rinsed nanoparticles that have been resdispersed in solutions of cetyltrimethylammonium bromide (CTAB). Both NBs and core−island-shell particles produce Rh NFWs, devoid of Pd, when etchant is added. The Rh nanoframework can be observed intact after etching of NBs, suggesting that the NB metal phases are separate in the structure.

The pure Pd, core−shell Pd−Rh, hollow Pd−Rh, and hollow Rh nanoparticles are uniform in size and shape after observation of many particles under TEM. Representative TEM images are shown in Figure 1a−h: (a,e) substrate Pd

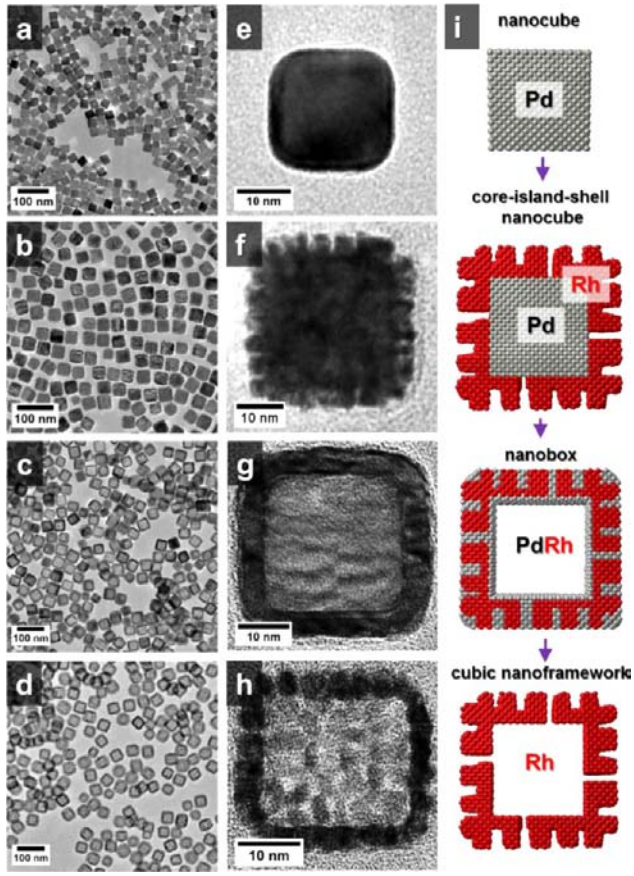

Figure 1. TEM images of (a,e) Pd nanocubes, (b,f) Pd−Rh core−island-shell nanocubes, (c,g) Pd−Rh NBs, and (d,h) Rh cubic NFWs. A scheme in panel i shows models for the structural evolution from Pd nanocube to Rh cubic NFW. The image in panel g contains a single Pd−Rh NB where contrast in the shell reveals the underlying Rh island framework in the structures.

NCs, (b,f) core−island-shell NCs, (c,g) NBs, and (d,h) hollow NFWs. Crystal model cross sections showing the proposed evolution from Pd cubes to Rh cubic frameworks are given in Figure 1i. It can be seen that the Rh cubic framework is left intact and the crystal domains are aligned. The fused regions are formed during the initial overgrowth. As the islands grew in size in the formation of the core−shell particles, they were epitaxial and made contact to form a porous yet, interconnected network of islands on the cube facets.

dx.doi.org/10.1021/ja405387q | J. Am. Chem. Soc. 2013, 135, 14691−14700

Figure 2a–c show additional TEM and HRTEM images of Pd–Rh NBs. The morphology is truncated cubic with a hollow

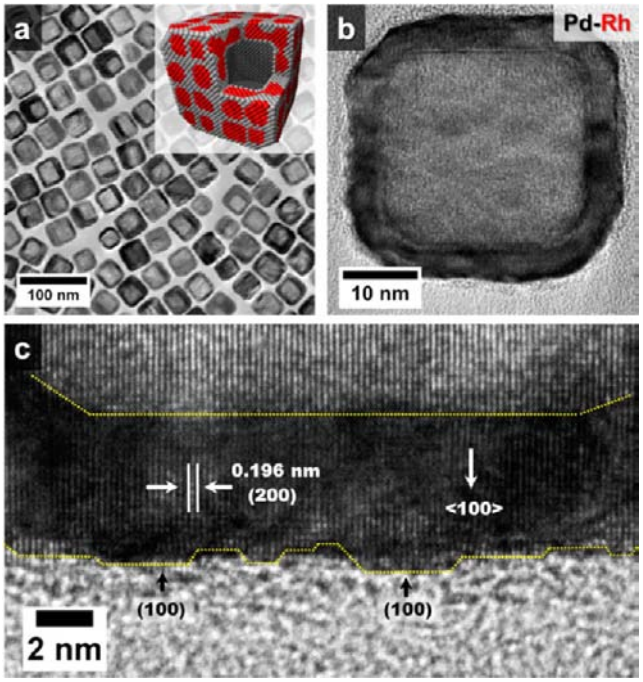

Figure 2. TEM and HRTEM images of Pd–Rh nanoboxes: (a) low-magnification image of Pd–Rh NBs with a crystal model inset, (b) high-magnification image of a single Pd–Rh NB, and (c) HRTEM image of the single-crystalline shell of the nanobox, which exhibits {100}-dominant faceting.

cubic interior. The shell is entirely filled and single crystalline. The migration was terminated at the outer edges of Rh island columns, corresponding with the known thickness (~4–5 nm) of the original Rh epigrowth. The cubic morphology indicates that the outer surfaces of these particles are dominated by {100} facets. Some {100}-terraces (along with steps in between) can be observed in the cross section of the HRTEM image of the shell in Figure 2c. This was the case across the majority of particles. A contrast variation throughout the TEM cross sections of the cube faces can be observed in the images. It could be contributed by the phase segregation of Pd and Rh. Supporting Information Figure S1a–c contains SEM images of Pd–Rh NBs and Rh NFWs and Supporting Information Figure S2a–d contains TEM images of NBs of different size and morphology that can also be synthesized by this route.

Controlling the migration of atoms in nanoparticles is a common feature to nanoparticle syntheses. Galvanic replacement, the Kirkendall effect, Ostwald ripening, oxidative etching, and surface detachment and readhesion mechanisms have all been used to control the atom migration in nanoparticles.[6,9,16,46,49−51] Preferential migration of one element to the particle surface under reducing or oxidizing environments has also been reported. This occurs because of fundamental differences in metal–metal bonding, metal surface free energy, and heats of formation of the corresponding surface metal oxide.[52−54] In our study, the mechanism of migration is unique. First, the Rh islands provide a framework matrix for Pd migration. This does not occur via galvanic replacement because of Pd's higher potential for reduction. Following, it is important to discuss the reason for the Rh nanoframeworks being left intact, both during the migration and after adding etchants. This is essentially a result of Rh's higher chemical stability. It is known that Pd dissolves in HCl at elevated temperatures, whereas Rh is resilient to the same treatment.[35] The fundamental explanation for the better chemical stability of Rh under such conditions can be explained by the higher Rh–Rh bond energy compared with Pd–Pd[55] and by the slower kinetics of halide complexation for Rh (kinetic stability of Rh). The halide ions have a preference for Pd because of a better "soft–soft" interaction compared with Rh.[35,36] In our synthesis, the Pd atoms or ions migrate from the particle cores via small gaps between the Rh islands in the shell, and this is accelerated by bromide ions supplied by CTAB present in the solution. Previously, Xie et al. have also invoked metal ion complexes in the explanation for oxidative etching of Pd in their recent work on the synthesis of Rh nanoframes.[48]

The chemical stability of Rh and Pd is understood, yet it is clear the formation of the Pd–Rh NBs involves more than oxidative etching of the Pd core. The Pd atoms or ions must diffuse along the surface and deposit between Rh islands in order to recapitulate a cubic particle with {100} facets. Recently, Yao et al. have suggested detachment–readhesion as a plausible theory for the relocation of metal atoms in single metal nanoparticle solutions.[49] Their study suggests that halide complexation is an important step in the mechanism. Tao et al. have, from another standpoint, discussed the preferential enrichment of the surface by one metal over the other depending on the redox environment above Pd–Rh bimetallic particles at high temperatures in gas phase.[52] They found that Rh prefers the surface in oxidative environments because of a lower heat of formation of the surface metal oxide (stability under oxidative gas environments). Pd only migrated to the surface when there was a reducing environment. This has been attributed to Pd's lower surface energy. We believe a combination of these processes dictates the formation of the Pd–Rh NBs. Since the solution of migration treatment is the original reaction solution, the combination of reducing environment (ascorbic acid in excess) and CTAB serves as a driving force for the Pd migration at raised temperature. The migration of Pd to the outer surfaces results in a box-like appearance that is the result of both the initial substrate morphology and the affinity of halides for the Pd and Rh {100} facets. Under oxidative conditions (when etchant is added), the Pd is not stable enough to remain in the nanostructure and is dissolved to yield pure Rh NFWs, which are chemically resistant to the treatment. The redox environment of the solution, the kinetic stability of Rh, and detachment–readhesion of Pd atoms mediated by bromide ions all play a role in the formation of the Pd–Rh NBs. The halides' occupation of {100} facets and the initial substrate's orientation both serve the important role of regenerating the cubic morphology.[48,49]

Control experiments were performed to confirm this mechanism for Pd migration and removal from the core–island-shell nanoparticles. Trimetallic particles containing Au were synthesized to discover whether more noble metals were unstable enough to be removed by the method. First, a layer of Pd was overgrown on Au seeds. These bimetallic nanoparticles were then used to overgrow Rh to create Au–Pd–Rh core–shell–island-shell trimetallic nanoparticles. The Au–Pd–Rh nanoparticles were washed and redispersed in CTAB solution and subjected to the identical oxidative conditions for

dx.doi.org/10.1021/ja405387q | J. Am. Chem. Soc. 2013, 135, 14691−14700

generating the Rh cubic NFWs. It was assumed that Au would be resilient to the etching treatment. This was confirmed by the resulting yolk–shell Au–Rh nanoparticles shown in Figure 3a,b, along with the synthetic scheme in Figure 3c. Pd was

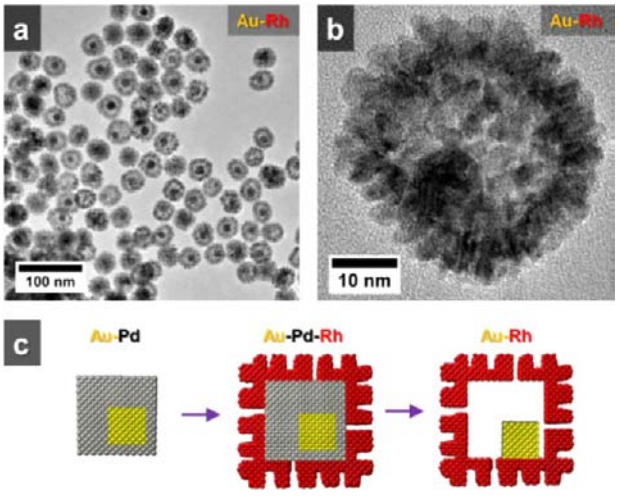

Figure 3. (a,b) TEM images of Au–Rh yolk–shell nanoparticles. A scheme is given in panel c for yolk–shell formation by selectively etching the Pd layer.

selectively removed from the inner shell layer of these particles, leaving the Au seed intact in the porous Rh shell. This process generated the Au–Rh yolk–shell type nanostructures. EDX measurements of the samples confirmed that the particles did not contain a significant amount of Pd after etching (Figure S8, Supporting Information). The experiments led to the conclusion that Pd is, again, unstable under the oxidative environment of these conditions. Gold, like rhodium, is resilient to the oxidation treatment, so the redox environment and the metal stability are important factors in the synthesis of NBs and NFWs. Additional control experiments involving the choice of etchant and other noble metals are shown in Supporting Information Figures S3 and S4. Supporting Information Figure S5 gives images for particles formed with the addition of excess halides and reducing agent to the washed nanoparticles instead of etchant. These experiments are not discussed here because they all agreed well with the presented mechanism. The formation of Rh NFWs beginning with Pd–Rh core–island-shell is depicted in more detail in Supporting Information Scheme S1.

To determine the crystal structures and degree of lattice strain on these structures, powder X-ray diffraction spectra were obtained for nanoparticle samples. The spectra obtained for Pd–Rh NBs and Rh NFWs are shown in Figure 4a along with peak positions of the pure metals from the structural database and a spectrum of the precursor core–island-shell structures. The peak positions do not overlay on the bulk angle positions. Even the Rh NFW peaks are shifted to lower angle positions compared with the bulk, most likely due to expansive lattice strain of Rh. It has been noted, however, that the 4d noble metals tend to relax away from their bulk positions at these size scales to a greater extent than their 5d counterparts.[37] A closer look at the spectra for the 220 peaks is given in Figure 4b. The single 220 peak at 69.60° for the Rh NFWs agrees with the EDX analysis that most of Pd is removed from the structure, so peaks at the Pd position do not show up in the spectrum for these single metal frameworks. The peak position of Rh NFWs

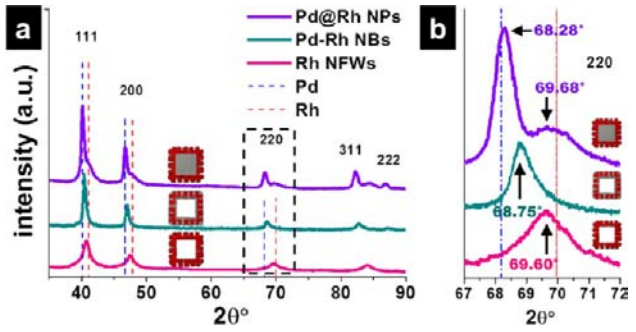

Figure 4. Powder XRD spectra of the Pd–Rh nanoparticles. Shown in panel a are spectra for Pd–Rh NPs, Pd–Rh nanoboxes, and Rh cubic nanoframeworks with monometallic bulk spectrum peak positions of both metals given for comparison. The 220 peak region is magnified and shown in panel b.

actually aligns well with the shoulder position (69.68°) from analysis of the core–island-shell nanoparticles. The Rh shoulder for the core–island-shell spectrum is broader than the Rh peak from NFWs indicating that there may be more variation in lattice parameters in the core–shell structure. This could be attributed to declining strain and influence of Pd at further distances from the core. Interestingly, only a single peak at 68.75° was observed for the Pd–Rh NBs.

The single 220 peak could suggest a homogeneous alloying of the metals in the shell, which conflicted with our expectation for segregation of the metal phases, so HAADF/STEM/EDX elemental mapping was used to gather more information. A clear distribution of Rh islands intact in the nanobox structure would confirm the proposed phase segregation. HAADF/STEM/EDX images and elemental maps were obtained for a single Pd–Rh nanobox and are provided in Figure 5a–e. It is clear from the elemental mapping that there is indeed phase segregation in the shell and that Pd is dispersed alternately between local Rh islands. This is evidenced by the nanoframework's appearance in the Rh map in Figure 5c and the overlay of Pd and Rh signals (shown in red and green, respectively) in Figure 5b, which shows the alternating arrangement of metal phases. Note that the images in Figure 5a–e are of a single NB viewed from the [110] zone axis. The proposed orientation of the particle is shown in models in Figure 5f,g and was achieved by tilting the sample in TEM. Best resolution of the alternating metal phases was obtained when the cube edge was viewed at this orientation of [110] zone axis. Interference from structures above and below the cross-section occurred when the NBs were oriented and viewed along the cube faces ([100] zone axis), so the contrast of phases is best at these thinner, exposed edges of the cube. The size of the Rh phases matches the size from the initial overgrowth structure of 4–5 nm. This information reaffirms the proposed structure and mechanism of Pd migration through gaps and channels left open from the initial Rh overgrowth and relocation at the external surface. The diffuse Pd map in Figure 5d shows that Pd has filled in the Rh island framework to regenerate the cube shape. The combined maps further validate our findings that the filling terminates with the Rh columns. This is important for catalysis studies because it suggests that both Pd and Rh {100} surfaces should be exposed on the NBs. Additionally, since HAADF/STEM/EDX, TEM, and HRTEM all show that the Rh framework is intact, we argue that either our laboratory-based powder XRD instrument (nonsynchrotron source) is not sensitive enough to

dx.doi.org/10.1021/ja405387q | J. Am. Chem. Soc. 2013, 135, 14691–14700

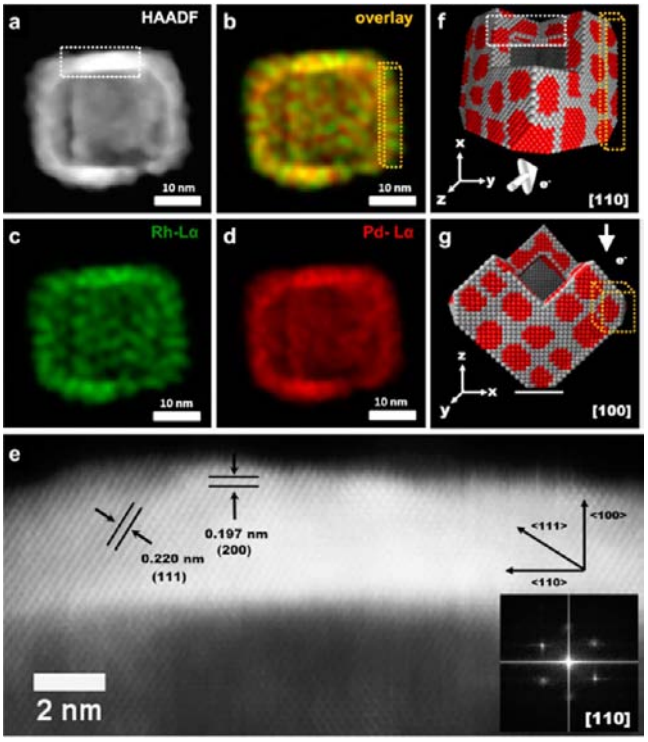

Figure 5. HAADF/STEM images and STEM/EDX elemental maps: (a) high angle annular dark-field image of a single Pd−Rh NB, (b) overlaid maps of Pd and Rh signals, (c) Rh contribution, (d) Pd contribution, and (e) a magnification of the section highlighted by the white, dashed box in panel a. Inset of panel e is FFT of the magnified image to show the crystal orientation. Panels f and g show nanocrystal models with the proposed orientation of the particle observed for STEM/EDX mapping.

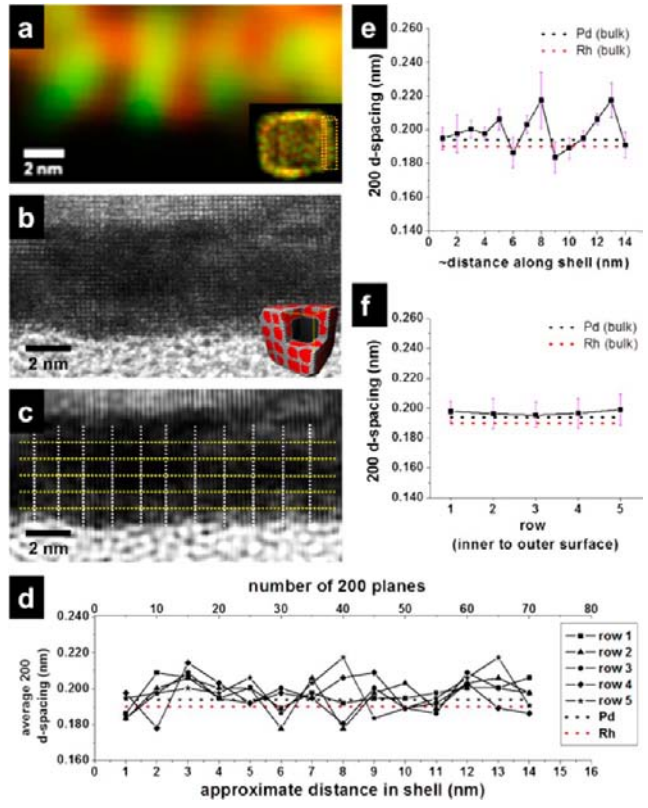

Figure 6. In panel a is a magnified STEM/EDX image of the shell region. In panel b is an HRTEM image of the shell of a single Pd−Rh nanobox. Panel c gives a FFT contrast-enhanced HRTEM image of the shell showing curvature of {200} planes with grid overlaid of the set of *d*-spacing measurements, which are plotted in panel d. Averaged *d*-spacing along and across the shell are given in panels e and f, respectively.

resolve segregation for phases at less than 5 nm or both phases are strained so that they give a single peak in XRD as what would be expected for a more homogeneous alloy.

Additional images of the Pd−Rh NB shell are shown in Figure 6a−c to elucidate the lattice parameters of the shell and to identify any strained features in the structure. Measurements of the *d*-spacing between {200} planes were obtained in Figure 6d from an FFT contrast-enhanced HRTEM image shown in Figure 6c. The FFT-enhanced image was generated from the HRTEM image in Figure 6b. Measurements in Figure 6d were made by averaging the *d*-spacing every five atomic planes for a total of 70 atomic planes (roughly ∼14 nm). This resulted in 14 averaged *d*-spacings along the shell. This was then repeated in a similar fashion until five rows of measurements were tabulated (from the interior to the exterior portion of the nanobox shell). While the *d*-spacing did vary along the shell, no noticeable trend could be observed. However, a significant difference in the lattice spacing for the {200} planes could be distinguished when measurements of each of the 14 columns and 5 rows were averaged (plotted in Figure 6e,f, respectively). The curve of lattice spacing traveling along the shell tends to oscillate, whereas, the spacing is somewhat constant going from the inner shell wall to the outer surface of the nanobox. The variation in lattice spacing results from the small mismatch (∼2%) of the two metal phases as they meet at several interfaces along the shell. This could be expected for an alternating arrangement of metal phases and is in line with the results of the previous analysis. Note that the relaxation of the lattice parameters for these metals at the nanoscale (*d*-spacings above the bulk values) has been experimentally observed and explained elsewhere.[37]

In addition to the lattice variation caused by alternating phases, defects or dislocations could be found in what appear to be channels utilized by Pd to fill the shell during diffusion to the exterior surface. This is shown in Figure 7a−d. FFT contrast-enhanced images of the shell shown in Figure 7b,d more clearly show a defect site. The edge dislocation highlighted is one of a few that could be observed from particle to particle and is likely due to the need to release lattice strain built up between the separate phases or any incomplete filling of the framework during Pd migration. Strain-releasing mechanisms in bimetallic NPs have been discussed in detail recently by Bhattari et al.[56]

Electrochemistry was used to test the catalytic behavior of the synthesized materials and to study effects of composition and lattice strain on catalysis arising from this archetype. A number of studies have been conducted recently on the effect of lattice strain for Pd,[57] Pt,[5] Pd−Pt alloy,[3,22] and Ru[58] as electrocatalysts but to our knowledge there has been no similar study for Rh. These studies cite the shift in d-band center due to lattice strain as the reason for enhanced or lessened catalytic activity. Expansion of the outer lattice shifts the d-band center upward, increasing the strength of chemisorption bonds, while compressing the outer lattice shifts the d-band center downward, in general weakening chemisorption bonds.[58] X-ray photoelectron spectroscopy (XPS) was carried out for the nanoparticle samples to probe the changes in Pd and Rh

dx.doi.org/10.1021/ja405387q | J. Am. Chem. Soc. 2013, 135, 14691−14700

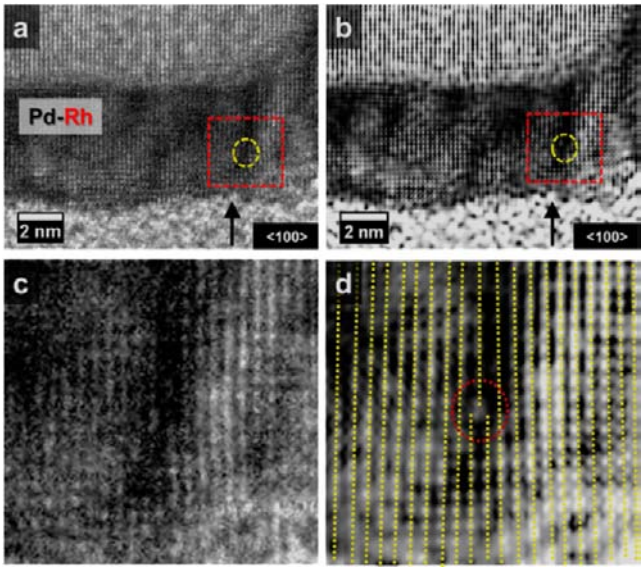

Figure 7. HRTEM image of (a) Pd−Rh hollow alloy nanocube shell and (c) magnified region showing a lattice dislocation. FFT contrast-enhanced HRTEM image of panel a is given in panel b, and panel d is the selected area of the image magnified to isolate the dislocation.

electronic structure due to lattice strain (Supporting Information Figure S6). The Pd and Rh 3d binding energies show a clear shift for both bimetallic structures compared with the pure Rh NFWs. Other groups have correlated these core-level shifts to a shift in the d-band center.[59,60] Incorporating a second metal into a metal nanostructure affects the catalytic activity via ensemble, ligand, and geometric strain effects, but strain is the only effect that can influence activity past a few atomic layers.[5] The impact of strain on the electrocatalytic activity of Rh NFWs and Pd−Rh NBs was studied alongside pure Pd nanocubes and Pd@Rh core−island-shell NPs for comparison.

Figure 8a shows results of CO stripping on the different nanoparticles, performed in a CO-saturated 0.1 M $HClO_4$ electrolyte solution. Core−island-shell Pd−Rh cubic NPs and pure Rh NFWs exhibit a nearly identical CO oxidation potential near 0.40 V vs SCE, pure Pd cubes reach peak oxidation potential at 0.72 V, and Pd−Rh NBs appear between these, near 0.55 V. These results suggest that the lattice strain of Rh has low impact on CO stripping activity and that the trend arises from composition. The core−shell particles should have a higher degree of lattice strain than the Rh NFWs, because the Pd core actively expands the Rh lattice. Both particle types exhibit the same CO stripping activity, however, indicating that lattice strain plays no significant role in this reaction. This result also indicates that the surface of the Pd−Rh core−island-shell NPs is mainly composed of Rh, with almost no Pd exposed. The Pd−Rh NB peak is between pure Pd and pure Rh, most likely due to a mixed composition at the surface.

Curves for the formic acid oxidation reaction (FOR) are given in Figure 8b. From lowest to highest activity (reverse scan current density), the particle types are Rh NFWs, Pd−Rh core−island-shell NPs, Pd−Rh NBs, and Pd nanocubes. This trend may be caused by the composition (amount of Pd), lattice strain, metal−metal interface, or a combination of the three. As stated earlier, Rh NFWs and Pd−Rh core−shell nanoparticles have the same CO stripping activity, indicating

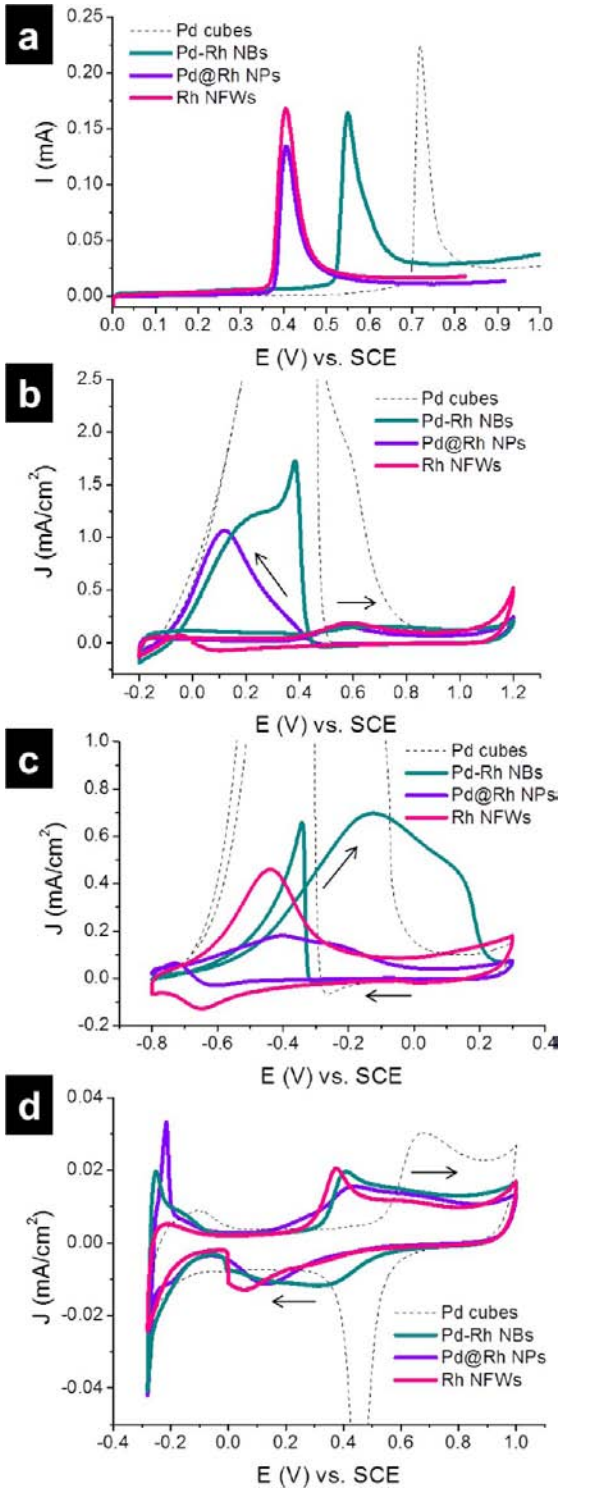

Figure 8. Cyclic voltammetry curves for electrochemical catalysis by Pd−Rh nanoparticles: (a) CO stripping, (b) formic acid oxidation, (c) alkaline ethanol oxidation, and (d) acidic ethanol oxidation for Pd cubes, Rh nanoframeworks, Pd−Rh core−island-shell nanocubes, and Pd−Rh alloy nanoboxes.

that the surface composition is the same; the Rh fused column layer is thick enough for Pd−Rh core−shell NPs that there is no Pd surface exposed. These two particle types, however, show vastly different activity for FOR. The Rh cubic NFWs have fractional current density, while Pd−Rh core−shell structures show a peak close to 1 mA/cm^2. The CO stripping result

dx.doi.org/10.1021/ja405387q | J. Am. Chem. Soc. 2013, 135, 14691−14700

eliminates Pd composition as a factor for FOR in this case, because the oxidation peaks had almost identical positions. Lattice strain can be invoked to explain the enhancement for Rh's FOR catalytic activity rather than composition or synergy. There are sequentially large increases in current density when considering Pd−Rh core−shell NPs, NBs, and pure Pd nanocubes. This trend matches an increasing degree of Pd composition and also follows the trend of increasing lattice strain. All of the particles comprising the Rh surface exhibit an indirect reaction pathway versus Pd's direct pathway. Rh typically follows an indirect pathway for FOR,[61] while Pd follows a direct pathway,[62] so in the case of Pd−Rh NBs, the FOR reaction is occurring either on the Rh surface or on a combination of Pd and Rh surfaces but is exhibiting predominantly Rh character. The absence of direct pathway in the NBs could be explained by the modification of the Pd lattice by Rh phases. Lattice strain likely affects FOR activity by increasing the adsorption of formic acid. On Rh, FOR proceeds by an indirect pathway: $HCOOH \rightarrow CO_{ads} + H_2O \rightarrow CO_2 + 2H^+ + 2e^-$.[63] In the first step, HCOOH is adsorbed as CO, and in the second step CO is oxidized to CO_2. The adsorption of HCOOH has been shown to be the rate-limiting step in FOR.[64] The upward shift in the d-band center due to lattice expansion increases the catalyst's ability to bind adsorbates. Norskov et al. showed that a higher d-band center leads to stronger chemisorption bonds,[58] and it has been shown that on a Pd(111) surface lattice expansion led to higher FOR activity due to stronger adsorption of HCOOH.[57] Unfortunately, because the adsorption step does not involve electron transfer, we cannot see a CV peak corresponding to HCOOH adsorption. Thus we can only infer an increased rate of adsorption by a higher peak on the reverse scan; the more HCOOH is adsorbed as CO, the more CO molecules are oxidized to CO_2, and a higher current is obtained. Accordingly we see that the particles with more strain have a higher oxidation peak on the reverse scan.

Ethanol oxidation reaction (EOR) was performed in both acidic and alkaline solutions. The EOR in an alkaline electrolyte tends to have higher activity than acidic EOR,[65] so we focus the discussion on the EOR in a solution of 1 M KOH + 1 M EtOH in order to determine the effect of lattice strain on EOR activity. The CV curves are shown in Figure 8c. The lowest current density is shown by the Pd−Rh core−shell NPs. The curve shows two adjacent peaks in the forward scan and a very small reverse scan peak. These characteristics are typical of a Rh alkaline EOR CV.[30] The pure Rh NFWs have a higher current density and a lower peak onset potential than core−shell NPs and do not exhibit the identifying Rh characteristics. The next highest current density is shown by Pd−Rh NBs, which have equally high forward and reverse scans, similar to Pd. EOR proceeds by a dual-pathway mechanism, either producing acetic acid and releasing only 4 electrons, or producing carbon dioxide and releasing 12 electrons.[66] Often, not all of the ethanol is completely oxidized to CO_2 on the forward scan, and the leftover incompletely oxidized products are oxidized further on the backward scan.[32] Thus, the ratio of the forward to backward current densities (j_f/j_b) can be used to compare the selectivity of the catalysts for the complete oxidation pathway, with a higher j_f/j_b value indicating a more selective catalyst. The j_f/j_b values for Pd NPs, Pd−Rh NBs, Pd−Rh core−shell NPs, and Rh NFWs are 0.809, 1.05, 2.55, and ∞, respectively (Rh NFWs have zero backward scan). These values indicate that the particles with more Rh have higher selectivity for the complete oxidation pathway. Looking at both the onset potentials and the j_f/j_b ratios, the less-strained particles with smaller surface lattices are better alkaline EOR catalysts. This trend is interestingly the opposite of the trend for FOR, demonstrating that these electrochemical reactions are uniquely sensitive to surface lattice strain and electronic structure. Even though the trend also correlates with decreasing Pd composition, composition alone cannot explain the trend. We can see by the different activities of Rh NFWs and Pd−Rh core−shell NPs, which have the same Rh surface composition as determined by CO stripping, that lattice strain must play a role in altering the kinetics of the reaction.

EOR was also performed in a perchloric acid electrolyte. There has been little research done on EOR in acidic media on Rh. One study compared EOR activity for Rh nanocubes, dendrites, and horned particles,[25] obtaining CVs similar to ours, shown in Figure 8d. Our results show similar current densities for Rh NFWs, Pd−Rh NBs, and core−shell NPs, with Pd cubes at a higher current density. According to Pd's higher intrinsic activity, we would expect to see higher activity for Pd−Rh NBs, which have some Pd exposed on the surface, but these particles have approximately the same current density as the other Rh-exposing structures, suggesting some degree of modification of Pd's lattice.

The oxygen reduction reaction (ORR) was the last electrochemical reaction tested, and the onset potentials are shown in Figure 9. This reaction interestingly does not follow

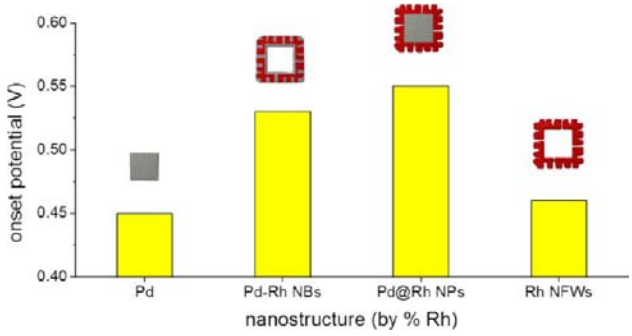

Figure 9. The onset potentials of the oxygen reduction reaction catalyzed by Pd−Rh nanoparticles.

the same trends in activity as for FOR or EOR. In the ORR, onset potential is used as the measure for catalytic performance. The Pd−Rh core−island-shell NPs are the most active at 0.55 V, followed by Pd−Rh NBs at 0.53 V, Rh NFWs at 0.46 V, and last Pd cubes at 0.45 V. For the ORR, pure Pd typically has low activity,[67] and our results show that by combining Pd with Rh to form bimetallic NPs, we can increase Pd's ORR activity. The Pd−Rh NBs have a higher onset potential than the Pd cubes, but a similar shaped curve indicating some Pd character in the reaction, shown in Supporting Information Figure S7a,b. The core−island-shell NPs, on the other hand, have a very different curve shown in Supporting Information, Figure S7c, with a large dip around 0.15 V that is characteristic of Rh due to the reduction of surface hydroxyls.[27] This dip shows that the core−shell NPs exhibit predominantly Rh character for this reaction, indicating that the surface is Rh and exposes little to no Pd. The pure Rh NFWs, however, show a lower onset potential (Supporting Information, Figure S7d). Because the surface composition for these two particle types is the same (as determined by CO stripping) but the activity is different, the

dx.doi.org/10.1021/ja405387q | J. Am. Chem. Soc. 2013, 135, 14691−14700

differing factor could be lattice strain. It has been shown that ORR activity can be altered by compressing the lattices of metal NPs.[5,68,69] The rate-limiting step for oxygen reduction is the desorption of O and OH from the metal surface, so a smaller lattice with a lower d-band center is ideal because it weakens chemisorption bonds, allowing O and OH to dissociate. A volcano relation was obtained for the onset potentials in the ORR for the different catalysts where the bimetallic structures display activity at higher voltage. An additional plot summarizing the activity for each of the nanocatalysts under each of the different reactions is given in Supporting Information, Figure 7e, for reference.

CONCLUSION

The synthesis and mechanism for the formation of Pd−Rh nanoboxes and Rh nanoframeworks was presented. The two different sets of cubic particles are generated by the heating of core−island-shell nanocubes under either reductive or oxidative environments. Detachment−readhesion mediated by bromide ions was discussed as the mechanism for the formation of the Pd−Rh NBs, with the chemical stability of each metal playing a major role in their formation. The synthesis utilizes Rh's preference for island growth, and Pd's reactivity to ligands and etchants to generate semiordered grid-like structures. The migration of Pd between Rh columns in the shell creates a phase-separated and strained heterostructure. The phases observed here (<5 nm phases) could only be resolved by advanced microscopy techniques. The Pd filling of the Rh island network to produce an alternating arrangement of metal phases at the surface is unprecedented in the literature. Extending this strategy yielded additional heterostructures, such as yolk−shell Au−Rh nanoparticles. Finally, the cubic nanoparticles' catalytic activities were investigated in model fuel cell reactions. It was discovered that lattice strain and composition at the surface were the most important factors influencing their catalytic behaviors, most notably in increasing Pd's performance as an ORR catalyst. For the purpose of studying the effects of lattice strain on catalysis, the grid-like nanobox architecture is of great interest. Future efforts are being directed toward other PGM and nonprecious metal systems where the migration mechanism could be utilized to create and study strain in nanocrystals that take on this new structural archetype.

METHODS

Chemicals and Materials. Rhodium(III) chloride hydrate ($RhCl_3{\cdot}nH_2O$, ∼40% Rh by wt), perchloric acid ($HClO_4$, 70%), hydrochloric acid (HCl, 37%), and formic acid (HCOOH, 95%) were all obtained from Sigma-Alrich. Sulfuric acid (H_2SO_4, 95%) was acquired from BDH. Cetyltrimethylammonium bromide (CTAB, 98%) was obtained from Calbiochem. Iron(III) chloride ($FeCl_3$, 98%) was obtained from Acros. Deionized water (18.2 MΩ) was used in all procedures. Rhodium(III) chloride hydrate was dissolved and diluted in water to yield 0.01 M $RhCl_3$. Solid $FeCl_3$ was dissolved in dilute HCl solution to give a 0.01 M solution of $FeCl_3$. Nitrogen and carbon monoxide were both obtained from Airgas.

Synthesis of Pd−Rh Nanoboxes. One reaction solution containing Pd−Rh core−island-shell nanocubes synthesized by our previously published procedure[31] was poured into a 50 mL glass pressure vessel directly after synthesis. The pressure vessel was sealed and placed in an oven set to 110 °C. The reaction was allowed to continue at this temperature for 48 h before removing the pressure vessel from the oven. After cooling to room temperature, the vessel was opened, and the particles were collected from centrifugation at 7000 rpm for 10 min. The particles were rinsed with DI water several times in this fashion in preparation for characterization and catalyst loading on electrodes. It was found that the synthesis of nanoboxes from core−island-shell nanoparticles with 0.200 mL of 0.01 M $RhCl_3$ for the overgrowth step in the original core−shell synthesis gave the most uniform nanoboxes.

Synthesis of Rh Nanoframeworks. The porous Rh frameworks were synthesized similarly to the Pd−Rh nanoboxes, but with the following exceptions. The core−island-shell nanocubes from one reaction solution were collected, centrifuged, and redispersed into a 10 mL solution of 0.05 g of CTAB in water *prior* to heating. This was done to remove the excess reducing agent in the original reaction solution. The solution containing the rinsed particles in CTAB was then poured into a 50 mL glass pressure vessel. Then 0.500 mL of etchant solution containing either 0.01 M $RhCl_3$ in water or 0.01 M $FeCl_3$ in dilute HCl (∼0.01 M) or dilute HCl was added. The particle solution was then heated for 48 h at 110 °C, and the particles were collected for characterization and catalysis in the same manner as described before for the nanoboxes. Note that the formation of Rh nanoframeworks occurs regardless of the size of the Rh overgrowth in the synthesis of the bimetallic core−island-shell nanocubes and independent of the etchant employed.

Characterization. Samples were prepared for transmission electron microscopy (TEM), scanning TEM (STEM), and energy-dispersive X-ray spectroscopy (EDX) by rinsing and redispersing nanoparticle solutions three times with DI water, and placing 1.0 μL droplets of nanoparticle solutions on carbon-coated copper grids. These were allowed to dry open to the air. The TEM was done using a JEOL JEM2010F accompanied by an EDX attachment operated at 200 kV. A Bruker AXS D2 Phaser diffractometer was used to obtain the powder X-ray diffraction patterns. Samples for XRD were prepared by placing 10 μL aliquots of concentrated nanoparticle solution on a glass slide and drying in air. The diffraction database structure identification numbers (for the fcc *d*-spacings) for Pd and Rh are 87-0645 and 87-07148, respectively.

STEM/EDX. High-resolution STEM and EDX mapping experiments were performed on a FEI Probe Cs corrected Titan operating at 200 kV.The high angle annular dark field (HAADF) images were acquired by a Fischione HAADF detector, and the EDX maps were acquired by ChemiSTEM technology with four windowless SDD detecors. This instrument incorporates the condenser spherical aberration corrector and X-FEG with probe current 0.4 nA in 0.31 nm spot and can achieve the resolution 0.08 nm as well as efficient X-ray collection rate.

Particle Cleaning and Electrode Preparation. Eight syntheses of Pd, core−shell, or hollow particles were centrifuged, combined, and redispersed to 10 mL. Before loading the particles onto the electrode, the particles were thoroughly cleaned to remove surface chemicals using a method previously reported by our group.[31] Five microliters of cleaned, concentrated particle solution was deposited onto the previously alumina-polished surface of a glassy carbon working electrode (CH Instruments). For oxygen reduction reaction (ORR) experiments, 20 μL of particle solution was deposited onto the surface of the rotating ring-disk electrode (RRDE).

Electrochemical Measurements. For CO stripping, formic acid oxidation, and ethanol oxidation reactions, a typical three-electrode system was used as previously reported.[31] First, 50 cycles of blank scans in 0.5 M H_2SO_4 were carried out at a scan rate of 100 mV/s from −0.2 to 1.0 V vs SCE. Next CO stripping and formic acid oxidation were performed as reported.[31] Ethanol oxidation was performed in a nitrogen-saturated 0.1 M EtOH + 0.1 M $HClO_4$ solution, scanning from −0.28 to 1.0 V vs SCE at a scan rate of 5 mV/s. Alkaline ethanol oxidation was performed in a 1 M KOH + 1 M EtOH solution, scanning from −0.8 to 0.3 V at a scan rate of 50 mV/s. Both formic acid and ethanol oxidation activities were normalized by electrochemically active surface area (ECSA) determined by CO stripping. For the ORR experiments, an RRDE-3A instrument (BioLogic) was used in conjunction with a platinum auxiliary electrode and saturated calomel reference electrode. The electrode was placed in nitrogen-saturated 0.1 M $HClO_4$ electrolyte and 50 cycles of blank scans were carried out at a scan rate of 100 mV/s from −0.2 to 1.0 V vs SCE. Next the electrode was placed in an oxygen-

saturated 0.1 M $HClO_4$ solution and rotated at a speed of 1600 rpm. Potential was cycled from 0.8 to 0.0 V at a scan rate of 5 mV/s.

■ ASSOCIATED CONTENT

Supporting Information

Additional TEM images, SEM images, XPS, and EDX measurements of the Pd−Rh NBs and Rh NFWs, plus those of particles formed in control experiments, images of alternate particle types that can be synthesized, a plot for the summary of activity in electrocatalysis, and a scheme depicting the formation mechanism. This material is available free of charge via the Internet at http://pubs.acs.org.

■ AUTHOR INFORMATION

Corresponding Author

frank.tsung@bc.edu

Author Contributions

†B. Sneed and C. Brodsky gave equal contributions to this work.

Notes

The authors declare no competing financial interest.

■ ACKNOWLEDGMENTS

Thanks to Boston College for funding the research. C.N.B. thanks the Northeast Section of the ACS (NESACS) for offering the Norris Richards Undergraduate Summer Research Scholarship. C.H.K. thanks the National Science Council in Taiwan for offering the scholarship. L.K.L. thanks BC for offering the John Kozarich Summer Undergraduate Research Fellowship. We also thank C. Dhital and the Wilson Group at BC for use of their diffractometer. F.F.T. thanks the Chemical Sciences, Geosciences and Biosciences Division, Office of Basic Energy Sciences, Office of Science, U.S. Department of Energy for the Grant No. DE-FG02-12ER1635.

■ REFERENCES

(1) Zaera, F. *Catal. Lett.* **2012**, *142*, 501.
(2) Koper, M. T. M. *Nanoscale* **2011**, *3*, 2054.
(3) Zhang, H.; Jin, M.; Xia, Y. *Chem. Soc. Rev.* **2012**, *41*, 8035.
(4) Wu, J.; Li, P.; Pan, Y.-T.; Warren, S.; Yin, X.; Yang, H. *Chem. Soc. Rev.* **2012**, *41*, 8066.
(5) Strasser, P.; Koh, S.; Anniyev, T.; Greeley, J.; More, K.; Yu, C.; Liu, Z.; Kaya, S.; Nordlund, D.; Ogasawara, H.; Toney, M. F.; Nilsson, A. *Nat. Chem.* **2010**, *2*, 454.
(6) González, E.; Arbiol, J.; Puntes, V. F. *Science* **2011**, *334*, 1377.
(7) Buck, M. R.; Schaak, R. E. *Angew. Chem., Int. Ed.* **2013**, *52*, 6154.
(8) Jiang, H.-L.; Xu, Q. *J. Mater. Chem.* **2011**, *21*, 13705.
(9) Hong, J. W.; Kang, S. W.; Choi, B.-S.; Kim, D.; Lee, S. B.; Han, S. W. *ACS Nano* **2012**, *6*, 2410.
(10) Huang, X.; Zhang, H.; Guo, C.; Zhou, Z.; Zheng, N. *Angew. Chem., Int. Ed.* **2009**, *48*, 4808.
(11) Song, H. M.; Anjum, D. H.; Sougrat, R.; Hedhili, M. N.; Khashab, N. M. *J. Mater. Chem.* **2012**, *22*, 25003.
(12) Bi, Y.; Lu, G. *Chem. Commun.* **2008**, 6402.
(13) Alayoglu, S.; Nilekar, A. U.; Mavrikakis, M.; Eichhorn, B. *Nat. Mater.* **2008**, *7*, 333.
(14) Nilekar, A. U.; Alayoglu, S.; Eichhorn, B.; Mavrikakis, M. *J. Am. Chem. Soc.* **2010**, *132*, 7418.
(15) Bauer, J. C.; Chen, X.; Liu, Q.; Phan, T.-H.; Schaak, R. E. *J. Mater. Chem.* **2008**, *18*, 275.
(16) Liu, J.; Qiao, S. Z.; Chen, J. S.; Lou, X. W.; Xing, X.; Lu, G. Q. *Chem. Commun.* **2011**, *47*, 12578.
(17) Kuo, C.-H.; Tang, Y.; Chou, L.-Y.; Sneed, B. T.; Brodsky, C. N.; Zhao, Z.; Tsung, C.-K. *J. Am. Chem. Soc.* **2012**, *134*, 14345.
(18) Wang, D.; Xin, H. L.; Hovden, R.; Wang, H.; Yu, Y.; Muller, D. A.; DiSalvo, F. J.; Abruña, H. D. *Nat. Mater.* **2013**, *12*, 81.
(19) Peng, Z.; Yang, H. *Nano Today* **2009**, *4*, 143.
(20) Stamenkovic, V. R.; Fowler, B.; Mun, B. S.; Wang, G.; Ross, P. N.; Lucas, C. A.; Marković, N. M. *Science* **2007**, *315*, 493.
(21) Singh, A. K.; Xu, Q. *ChemCatChem* **2013**, *5*, 652.
(22) Deng, Y.-J.; Tian, N.; Zhou, Z.-Y.; Huang, R.; Liu, Z.-L.; Xiao, J.; Sun, S.-G. *Chem. Sci.* **2012**, *3*, 1157.
(23) Lim, B.; Jiang, M.; Camargo, P. H. C.; Cho, E. C.; Tao, J.; Lu, X.; Zhu, Y.; Xia, Y. *Science* **2009**, *324*, 1302.
(24) Zhang, Y.; Janyasupab, M.; Liu, C.-W.; Li, X.; Xu, J.; Liu, C.-C. *Adv. Funct. Mater.* **2012**, *22*, 3570.
(25) Yuan, Q.; Zhou, Z.; Zhuang, J.; Wang, X. *Inorg. Chem.* **2010**, *49*, 5515.
(26) Park, K.-W.; Han, D.-S.; Sung, Y.-E. *J. Power Sources* **2006**, *163*, 82.
(27) Cao, D.; Wieckowski, A.; Inukai, J.; Alonso-Vante, N. *J. Electrochem. Soc.* **2006**, *153*, A869.
(28) Kiran, V.; Ravikumar, T.; Kalyanasundaram, N. T.; Krishnamurty, S.; Shukla, A. K.; Sampath, S. *J. Electrochem. Soc.* **2010**, *157*, B1201.
(29) Sathe, B. R.; Balan, B. K.; Pillai, V. K. *Energy Environ. Sci.* **2011**, *4*, 1029.
(30) Suo, Y.; Hsing, I. M. *J. Power Sources* **2011**, *196*, 7945.
(31) Sneed, B. T.; Kuo, C.-H.; Brodsky, C. N.; Tsung, C.-K. *J. Am. Chem. Soc.* **2012**, *134*, 18417.
(32) Shen, S.; Zhao, T. *J. Mater. Chem. A* **2013**, *1*, 906.
(33) Balan, B. K.; Sathe, B. R. *J. Nanosci. Nanotechnol.* **2012**, *12*, 8994.
(34) Tedsree, K.; Chan, C. W. A.; Jones, S.; Cuan, Q.; Li, W.-K.; Gong, X.-Q.; Tsang, S. C. E. *Science* **2011**, *332*, 224.
(35) Renner, H.; Schlamp, G.; Kleinwächter, I.; Drost, E.; Lüschow, H. M.; Tews, P.; Panster, P.; Diehl, M.; Lang, J.; Kreuzer, T.; Knödler, A.; Starz, K. A.; Dermann, K.; Rothaut, J.; Drieselmann, R.; Peter, C.; Schiele, R. *Ullmann's Encyclopedia of Industrial Chemistry*; Wiley-VCH Verlag GmbH & Co. KGaA: Weinheim, Germany, 2000.
(36) Bernardis, F. L.; Grant, R. A.; Sherrington, D. C. *React. Funct. Polym.* **2005**, *65*, 205.
(37) Sanchez, S. I.; Small, M. W.; Bozin, E. S.; Wen, J.-G.; Zuo, J.-M.; Nuzzo, R. G. *ACS Nano* **2012**, *7*, 1542.
(38) Kobayashi, H.; Lim, B.; Wang, J.; Camargo, P. H. C.; Yu, T.; Kim, M. J.; Xia, Y. *Chem. Phys. Lett.* **2010**, *494*, 249.
(39) Ewers, T. D.; Sra, A. K.; Norris, B. C.; Cable, R. E.; Cheng, C.-H.; Shantz, D. F.; Schaak, R. E. *Chem. Mater.* **2005**, *17*, 514.
(40) Long, N. V.; Chien, N. D.; Hirata, H.; Matsubara, T.; Ohtaki, M.; Nogami, M. *J. Cryst. Growth* **2011**, *320*, 78.
(41) Hoefelmeyer, J. D.; Niesz, K.; Somorjai, G. A.; Tilley, T. D. *Nano Lett.* **2005**, *5*, 435.
(42) Biacchi, A. J.; Schaak, R. E. *ACS Nano* **2011**, *5*, 8089.
(43) Zhang, Y.; Grass, M. E.; Kuhn, J. N.; Tao, F.; Habas, S. E.; Huang, W.; Yang, P.; Somorjai, G. A. *J. Am. Chem. Soc.* **2008**, *130*, 5868.
(44) Suntivich, J.; Xu, Z.; Carlton, C. E.; Kim, J.; Han, B.; Lee, S. W.; Bonnet, N.; Marzari, N.; Allard, L. F.; Gasteiger, H. A.; Hamad-Schifferli, K.; Shao-Horn, Y. *J. Am. Chem. Soc.* **2013**, *135*, 7985.
(45) Tao, F.; Dag, S.; Wang, L. W.; Liu, Z.; Butcher, D. R.; Bluhm, H.; Salmeron, M.; Somorjai, G. A. *Science* **2010**, *327*, 850.
(46) Tao, F.; Grass, M. E.; Zhang, Y.; Butcher, D. R.; Aksoy, F.; Aloni, S.; Altoe, V.; Alayoglu, S.; Renzas, J. R.; Tsung, C.-K.; Zhu, Z.; Liu, Z.; Salmeron, M.; Somorjai, G. A. *J. Am. Chem. Soc.* **2010**, *132*, 8697.
(47) Zhang, H.; Jin, M.; Liu, H.; Wang, J.; Kim, M. J.; Yang, D.; Xie, Z.; Liu, J.; Xia, Y. *ACS Nano* **2011**, *5*, 8212.
(48) Xie, S.; Lu, N.; Xie, Z.; Wang, J.; Kim, M. J.; Xia, Y. *Angew. Chem., Int. Ed.* **2012**, *51*, 10266.
(49) Yao, S.; Yuan, Y.; Xiao, C.; Li, W.; Kou, Y.; Dyson, P. J.; Yan, N.; Asakura, H.; Teramura, K.; Tanaka, T. *J. Phys. Chem. C* **2012**, *116*, 15076.
(50) Vasquez, Y.; Henkes, A. E.; Chris Bauer, J.; Schaak, R. E. *J. Solid State Chem.* **2008**, *181*, 1509.

(51) Schaak, R. E.; Sra, A. K.; Leonard, B. M.; Cable, R. E.; Bauer, J. C.; Han, Y.-F.; Means, J.; Teizer, W.; Vasquez, Y.; Funck, E. S. *J. Am. Chem. Soc.* **2005**, *127*, 3506.
(52) Tao, F.; Grass, M. E.; Zhang, Y.; Butcher, D. R.; Renzas, J. R.; Liu, Z.; Chung, J. Y.; Mun, B. S.; Salmeron, M.; Somorjai, G. A. *Science* **2008**, *322*, 932.
(53) Wang, L.-L.; Johnson, D. D. *J. Am. Chem. Soc.* **2009**, *131*, 14023.
(54) Ruban, A. V.; Skriver, H. L.; Nørskov, J. K. *Phys. Rev. B* **1999**, *59*, 15990.
(55) Harada, M.; Asakura, K.; Ueki, Y.; Toshima, N. *J. Phys. Chem.* **1993**, *97*, 10742.
(56) Bhattarai, N.; Casillas, G.; Ponce, A.; Jose-Yacaman, M. *Surf. Sci.* **2013**, *609*, 161.
(57) Kibler, L. A.; El-Aziz, A. M.; Hoyer, R.; Kolb, D. M. *Angew. Chem., Int. Ed.* **2005**, *44*, 2080.
(58) Mavrikakis, M.; Hammer, B.; Nørskov, J. K. *Phys. Rev. Lett.* **1998**, *81*, 2819.
(59) Richter, B.; Kuhlenbeck, H.; Freund, H. J.; Bagus, P. S. *Phys. Rev. Lett.* **2004**, *93*, No. 026805.
(60) Zhou, W. P.; Lewera, A.; Larsen, R.; Masel, R. I.; Bagus, P. S.; Wieckowski, A. *J. Phys. Chem. B* **2006**, *110*, 13393.
(61) Adić, R. R.; Tripković, A. V. *J. Electroanal. Chem. Interfacial Electrochem.* **1979**, *99*, 43.
(62) Rice, C.; Ha, S.; Masel, R. I.; Wieckowski, A. *J. Power Sources* **2003**, *115*, 229.
(63) Grozovski, V.; Solla-Gullón, J.; Climent, V. c.; Herrero, E.; Feliu, J. M. *J. Phys. Chem. C* **2010**, *114*, 13802.
(64) Xiang, J.; Wu, B.-L.; Chen, S.-L. *J. Electroanal. Chem.* **2001**, *517*, 95.
(65) Lai, S. C. S.; Kleijn, S. E. F.; Öztürk, F. T. Z.; van Rees Vellinga, V. C.; Koning, J.; Rodriguez, P.; Koper, M. T. M. *Catal. Today* **2010**, *154*, 92.
(66) Lai, S. C. S.; Koper, M. T. M. *Phys. Chem. Chem. Phys.* **2009**, *11*, 10446.
(67) Savadogo, O.; Lee, K.; Oishi, K.; Mitsushima, S.; Kamiya, N.; Ota, K. I. *Electrochem. Commun.* **2004**, *6*, 105.
(68) Wang, J. X.; Inada, H.; Wu, L.; Zhu, Y.; Choi, Y.; Liu, P.; Zhou, W.-P.; Adzic, R. R. *J. Am. Chem. Soc.* **2009**, *131*, 17298.
(69) Zhang, J.; Vukmirovic, M. B.; Xu, Y.; Mavrikakis, M.; Adzic, R. R. *Angew. Chem.* **2005**, *117*, 2170.